Available online at www.sciencedirect.com
SCIENCE DIRECT®
Ocean Modelling 7 (2004) 39–58
Ocean Modelling
www.elsevier.com/locate/ocemod

Advection schemes for unstructured grid ocean modelling

E. Hanert [a,b,*], D.Y. Le Roux [c], V. Legat [b], E. Deleersnijder [a]

[a] *Institut d'Astronomie et de Géophysique G. Lemaître, Université Catholique de Louvain, 2 Chemin du Cyclotron, B-1348 Louvain-la-Neuve, Belgium*

[b] *Centre for Systems Engineering and Applied Mechanics, Université Catholique de Louvain, 4 Avenue Georges Lemaître, B-1348 Louvain-la-Neuve, Belgium*

[c] *Département de Mathématiques et de Statistique, Université Laval, Québec, QC, Canada, G1K 7P4*

Received 21 March 2003; received in revised form 2 May 2003; accepted 2 May 2003

Abstract

We study advection schemes for unstructured grid ocean models. Four linear advection schemes are investigated by solving a scalar transport equation. Schemes under consideration include continuous, non-conforming and discontinuous finite elements and finite volumes. A comprehensive derivation of the numerical schemes is presented and conservation and dispersion properties are discussed. An assessment is made by performing the test problem introduced by Hecht et al. [J. Geophys. Res. 100 (1995) 20763] in which a passive scalar field is advected through an analytical Stommel gyre. It is found that continuous finite elements and finite volumes have some difficulties to represent accurately solutions with steep gradients. As a result they are prone to generate unphysical oscillations. On the other hand, discontinuous and non-conforming finite element schemes perform better. This is due to their higher flexibility that makes them better suited to highly sheared flows.

Keywords: Unstructured grids; Advection schemes

1. Introduction

Ocean circulation strongly depends on water density gradients. Empirical parameterizations permit to express water density in terms of water temperature and salinity. These quantities are

* Corresponding author. Address: Institut d'Astronomie et de Géophysique G. Lemaître, Université Catholique de Louvain, 2 Chemin du Cyclotron, B-1348 Louvain-la-Neuve, Belgium. Tel.: +32-10-47-23-54; fax: +32-10-47-47-22.
E-mail address: hanert@astr.ucl.ac.be (E. Hanert).

1463-5003/$ - see front matter
doi:10.1016/S1463-5003(03)00029-5

transported by the flow and diffused by eddy mixing. Their evolution is thus governed by an advection–diffusion equation. Since this equation is usually dominated by advection, it is especially important that numerical models accurately represent advective processes. This is however not straightforward, especially with Eulerian schemes.

The vast majority of ocean models use a structured grid and the finite difference method. This is mainly due to the inherent simplicity of structured grids. Nevertheless, in the last years much attention has been paid to unstructured grids (e.g. Le Provost et al., 1994; Myers and Weaver, 1995; Lynch et al., 1996; Le Roux et al., 2000; Nechaev et al., 2003; Danilov et al., 2003). Their ability to represent complex geometries and localized phenomena sounds attractive given the high complexity of oceanic flows.

In unstructured grid ocean modelling, the numerical treatment of advection is still a central issue. The choice of a convenient numerical method has not been thoroughly discussed yet and many advection schemes commonly used in engineering seem to be ignored by ocean modellers. A convenient scheme should involve a compromise between quality and computational cost. The quality of the solution must be assessed in the context of ocean modelling.

In the present paper, we evaluate four linear advection schemes applied to two-dimensional tracer transport within a Stommel gyre. This test problem is relevant in ocean modelling where intense boundary flows with strong shear are often constraining for numerical methods. Herein we consider finite volumes and continuous, discontinuous and non-conforming finite elements. They are quite representative of available Eulerian methods for unstructured grids.

Among the four methods examined in the present paper, continuous finite elements are the most often used in unstructured grid ocean models. They may be stabilized with Galerkin least-squares (Danilov et al., 2003) or pseudo residual-free bubble functions (Nechaev et al., 2003) to obtain better results. Finite volumes are well suited to solve conservative law problems. They are based on a decomposition of the computational domain into control volumes and on flux budgets between those volumes. More details may be found in Le Veque (2002). Discontinuous finite elements were first analysed by Le Saint and Raviart (1974). They have been studied intensively in the last decade and applied to a large number of problems. A comprehensive review may be found in Cockburn et al. (2000). Non-conforming finite elements have been introduced by Crouzeix and Raviart (1973) to solve Stokes equations. They have proved to be well suited to represent shallow water oceanic flows (Hua and Thomasset, 1984; Le Roux, 2003).

The paper is organized as follows. We first present the model problem and domain partitions in Sections 2 and 3. The weak formulation is introduced in Section 4 and the discrete equations are derived in Section 5. Conservation and dispersion properties are discussed in Sections 6 and 7. Section 8 presents numerical experiments and a discussion of the methods performances with the test case of Hecht et al. (1995). Conclusions are given in Section 9.

2. Continuous problem

We consider the following advection–diffusion problem: Let Ω be an open bounded domain in $\mathbf{R}^n$ $(n = 2, 3)$, we seek the scalar function $s(\mathbf{x}, t)$ which is the solution of the following boundary value problem:

$$\frac{\partial s}{\partial t} + \nabla \cdot (\mathbf{u}s) = \nabla \cdot (K \nabla s) \quad \text{on } \Omega, \ \forall t, \tag{1}$$

$$K \nabla s \cdot \mathbf{n} = 0 \quad \text{on } \partial\Omega, \tag{2}$$

$$s(\mathbf{x}, 0) = s_0(\mathbf{x}) \quad \text{on } \Omega, \tag{3}$$

where $\partial\Omega \subset \mathbf{R}^{n-1}$ is the domain boundary, $\mathbf{u} = \mathbf{u}(\mathbf{x})$ is a given divergence-free velocity field such that $\mathbf{u} \cdot \mathbf{n} = 0$ on $\partial\Omega$, $\mathbf{n}$ is the unit normal vector pointing out of the domain Ω and K is a constant diffusion coefficient.

3. Domain partitions

Let $\mathscr{P}$ be a partition of the domain Ω into N_Ω disjoint open subdomains Ω_i:

$$\overline{\Omega} = \bigcup_{i=1}^{N_\Omega} \overline{\Omega}_i \quad \text{and} \quad \Omega_i \cap \Omega_j = \emptyset \quad \text{for } i \neq j.$$

The notation $\overline{\Omega}$ represents the closure of Ω. Each subdomain Ω_i has a boundary $\partial\Omega_i$. Let Γ be the ensemble of interelement boundaries $\Gamma_l = \partial\Omega_i \cap \partial\Omega_j$ with $i > j$ inside the domain, with all possible combinations:

$$\overline{\Gamma} = \bigcup_{l=1}^{N_\Gamma} \overline{\Gamma}_l \quad \text{and} \quad \Gamma_l \cap \Gamma_m = \emptyset \quad \text{for } l \neq m,$$

where N_Γ is the number of elements in Γ. With each $\Gamma_l \in \Gamma$ we associate a unique unit normal vector $\mathbf{n}$ which points from Ω_i to Ω_j. We also build a triangulation of Ω such that each element E_e belongs to only one subdomain Ω_i. Hence the domain Ω is such that:

$$\overline{\Omega} = \bigcup_{e=1}^{N_\mathrm{E}} \bar{E}_e \quad \text{and} \quad E_e \cap E_f = \emptyset \quad \text{for } e \neq f,$$

where N_E is the number of triangles in Ω. The total number of vertices and segments in the triangulation are denoted N_V and N_S. An illustration of the different partitions is given in Fig. 1.

In the present paper we also consider a finite volume scheme and thus introduce a partition of the computational domain Ω into disjoint open control volumes V_n:

$$\overline{\Omega} = \bigcup_{n=1}^{N_\mathrm{V}} \bar{V}_n \quad \text{and} \quad V_n \cap V_p = \emptyset \quad \text{for } n \neq p.$$

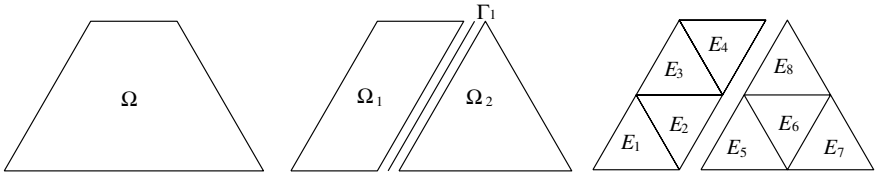

Fig. 1. Example of partition of the domain Ω into two subdomains Ω_1 and Ω_2. The segment between Ω_1 and Ω_2 is denoted Γ_1. Each subdomain is partitioned into triangles E_e ($1 \leqslant e \leqslant 8$). For the present example, $N_\Omega = 2$, $N_\Gamma = 1$, $N_\mathrm{E} = 8$, $N_\mathrm{V} = 9$ and $N_\mathrm{S} = 16$.

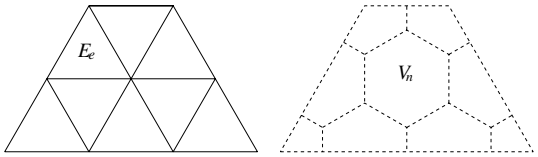

Fig. 2. Partitions of Ω into triangles (left) and the corresponding control volumes partition (right). The control volumes (dashed lines) are built by joining the barycenter of each triangle to the center of the three faces.

Control volumes are built by joining the barycenter of each triangle E_e to the centres of the three faces (Fig. 2). Such a partition of Ω corresponds to the Voronoï diagram of the triangulation if the latter is a Delaunay triangulation.

4. A non-continuous variational or weak formulation

We now proceed with the derivation of a non-continuous weak formulation of problem (1) on a partitioned domain Ω. First of all we multiply (1) with a test function $\hat{s}$ belonging to a function space $\mathscr{S} = \{v \in L^2(\Omega) : v_{|\Omega_i} \in H^1(\Omega_i),\ \forall \Omega_i \in \mathscr{P}\}$. The equation is then integrated by parts on the partition $\mathscr{P}$ of Ω:

$$\sum_{i=1}^{N_\Omega} \int_{\Omega_i} \left(\frac{\partial s}{\partial t}\hat{s} - s\mathbf{u}\cdot\nabla\hat{s} + K\nabla s\cdot\nabla\hat{s} \right) \mathrm{d}\Omega + \sum_{l=1}^{N_\Gamma} \int_{\Gamma_l} \{\langle s\mathbf{u}\cdot\mathbf{n}\rangle[\hat{s}] + [s\mathbf{u}\cdot\mathbf{n}]\langle\hat{s}\rangle\}\,\mathrm{d}\Gamma - \sum_{l=1}^{N_\Gamma} \int_{\Gamma_l} \{\langle K\nabla s\cdot\mathbf{n}\rangle[\hat{s}] + [K\nabla s\cdot\mathbf{n}]\langle\hat{s}\rangle\}\,\mathrm{d}\Gamma = 0, \tag{4}$$

where $[f] = f_{|\Omega_i} - f_{|\Omega_j}$ and $\langle f\rangle = \frac{1}{2}(f_{|\Omega_i} + f_{|\Omega_j})$ respectively denote the jump and average of f on an interior edge Γ_l. The restriction of f on Ω_i is denoted $f_{|\Omega_i}$.

The weak formulation is obtained by adding weak continuity constraints to Eq. (4). This is due to the elliptic nature of the problem which requires the continuity of the solution values and diffusive fluxes between subdomains. Hence, the weak formulation reads:

Find $s(\mathbf{x}, t) \in \mathscr{S}$ such that

$$\sum_{i=1}^{N_\Omega} \int_{\Omega_i} \left(\frac{\partial s}{\partial t}\hat{s} - s\mathbf{u}\cdot\nabla\hat{s} + K\nabla s\cdot\nabla\hat{s} \right) \mathrm{d}\Omega + \sum_{l=1}^{N_\Gamma} \int_{\Gamma_l} \{\langle s\mathbf{u}\cdot\mathbf{n}\rangle[\hat{s}] + [s\mathbf{u}\cdot\mathbf{n}]\langle\hat{s}\rangle\}\mathrm{d}\Gamma - \sum_{l=1}^{N_\Gamma} \int_{\Gamma_l} \{\langle K\nabla s\cdot\mathbf{n}\rangle[\hat{s}] + [K\nabla s\cdot\mathbf{n}]\langle\hat{s}\rangle\}\mathrm{d}\Gamma + \sum_{l=1}^{N_\Gamma} \int_{\Gamma_l} \{[s][a(\hat{s})] + 2[K\nabla s\cdot\mathbf{n}]\langle b(\hat{s})\rangle\}\mathrm{d}\Gamma = 0 \quad \forall \hat{s} \in \mathscr{S}. \tag{5}$$

The functions $a(\hat{s})$ and $b(\hat{s})$ can be selected to weigh the importance of the continuity constraints versus the advection–diffusion equation. Let us emphasize that continuity constraints are only weakly satisfied by the solution of problem (5). The solution of the weak formulation that we

derived is not continuous between subdomains. However, the solution of the strong formulation or classical weak formulation belongs to $H^1(\Omega)$. In such a formulation, strong enforcement of the continuity of the solution and weak continuity of the fluxes is automatically obtained, without the need to add penalty terms. Algebraic details, about the way Eq. (4) and problem (5) are derived, are given in Appendix A.

Elliptic problems require the continuity of the solution in all directions while purely hyperbolic problems only require continuity along characteristics. In order to meet those demands, we consider the following expression for $a(\hat{s})$:

$$a(\hat{s}) = \begin{cases} \frac{K}{|\Gamma_l|}\hat{s} + \mathbf{u}\cdot\mathbf{n}(\lambda - 1/2)\hat{s} & \text{on } \Omega_i, \\ \frac{K}{|\Gamma_l|}\hat{s} + \mathbf{u}\cdot\mathbf{n}(\lambda + 1/2)\hat{s} & \text{on } \Omega_j, \end{cases}$$

where $|\Gamma_l|$ is the measure of Γ_l. The first term in the expression of $a(\hat{s})$ enforces the continuity of the solution in all directions (Houston et al., 2000). It depends on the diffusion coefficient in order to increase the constraint as diffusion increases. The second term only demands the continuity of the solution values along characteristics. This amounts to impose the continuity of the advective fluxes. The latter constraint is the only one which remains when $K = 0$. The parameter $\lambda \in [-1/2, 1/2]$ permits to orient the advective flux. A centered advection scheme is obtained by choosing $\lambda = 0$. Such a scheme is not the best suited to strongly advective flows since it is directionally symmetric contrary to advection. As a result, it may easily generate false extrema. A more stable scheme can be derived by taking into account the directionally oriented nature of the flow and thus selecting $\lambda = \frac{1}{2}\text{sign}(\mathbf{u}(\mathbf{x})\cdot\mathbf{n}(\mathbf{x}))$. This can be interpreted as an upwind scheme that permits to avoid many unphysical ripples in the solution. This parametrization will be used from now on to discretize the advective flux. To discretize the diffusive fluxes, we assume that diffusion is an isotropic phenomenon. Hence the diffusive flux continuity constraint should not be oriented and we choose:

$$b(\hat{s}) = \hat{s}/2.$$

For a 3D oceanic flow, horizontal and vertical diffusivities are usually different and an other expression for $b(\hat{s})$ should then be selected. There are of course many possibilities for $a(\hat{s})$ and $b(\hat{s})$ which give different formulations.

Finally, the weak or variational formulation of the boundary value problem reads:

Find $s(\mathbf{x}, t) \in \mathscr{S}$ such that

$$\sum_{i=1}^{N_\Omega} \int_{\Omega_i} \left(\frac{\partial s}{\partial t}\hat{s} - s\mathbf{u}\cdot\nabla\hat{s} + K\nabla s\cdot\nabla\hat{s} \right) \mathrm{d}\Omega + \sum_{l=1}^{N_\Gamma} \int_{\Gamma_l} \left(\langle s\mathbf{u}\cdot\mathbf{n}\rangle_\lambda [\hat{s}] - \langle K\nabla s\cdot\mathbf{n}\rangle [\hat{s}] + \frac{K}{|\Gamma_l|}[s][\hat{s}] \right) \mathrm{d}\Gamma = 0 \quad \forall \hat{s} \in \mathscr{S}, \tag{6}$$

where $\langle f\rangle_\lambda$ denotes the weighed average of f on the segment Γ_l:

$$\langle f\rangle_\lambda = (1/2 + \lambda) f_{|\Omega_i} + (1/2 - \lambda) f_{|\Omega_j}.$$

The variational formulation (6) involves the computation of upwind advective fluxes and centered diffusive fluxes on the interfaces between subdomains. It also involves the computation of a weak continuity constraint term to prevent sharp discontinuities in the solution while solving elliptic problems.

5. Discrete equations

We now construct a approximation s^h to the exact solution of problem (1)–(3) in a finite dimensional space $\mathscr{S}^h \subset \mathscr{S}$:

$$s \approx s^h = \sum_{i=1}^{N} S_i \phi_i,$$

where S_i and ϕ_i are the nodal value and the basis function associated with node i respectively. The number of nodal values is denoted N. In the present paper, we only consider continuous, discontinuous and non-conforming linear approximations. The shape functions used for those approximations are represented on Fig. 3. A shape function is always equal to one on the associated node and equal to zero on any other node. As seen in Fig. 4, the nodal values of the continuous approximation are lying on the vertices of the triangulation and thus belong to many elements. The discrete solution is therefore continuous between triangles. For the discontinuous approximation, the nodal values still lie on the vertices of the triangulation but entirely belong to a particular element of the mesh. This approximation is thus completely discontinuous between triangles and information propagates only through fluxes between adjacent elements. The nodal values of the non-conforming approximation are lying in the middle of the segments of the triangulation. This discrete solution is only continuous across triangle boundaries at mid-side nodes and discontinuous everywhere else around a triangle boundary.

We shall consider a partition $\mathscr{P}$ of Ω such that the restriction of s^h on $\mathscr{P}$ is continuous. In our presentation, there is only one subdomain for continuous approximations and N_E subdomains for discontinuous and non-conforming approximations. Discontinuous and non-conforming schemes are thus obtained by considering that each element of the triangulation is a subdomain Ω_i and that $s^h_{|\Omega_i}$ is continuous. It should be noted that an equivalent approach would be to assume that there is only one subdomain $\Omega_1 = \Omega$ but that s^h may be discontinuous between triangles.

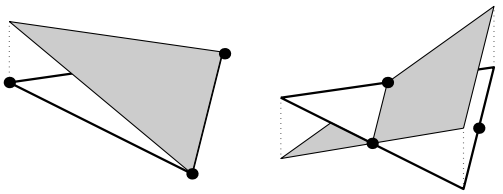

Fig. 3. Shape functions (in gray) associated with continuous and discontinuous approximations (left) and non-conforming approximations (right).

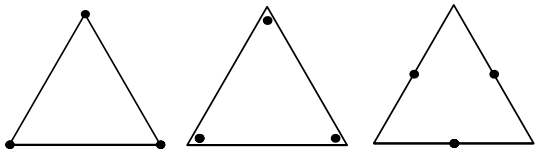

Fig. 4. Nodal values (•) distributions for the linear continuous (left), discontinuous (centre) and non-conforming (right) approximations.

A finite element approximation to the exact solution of problem (1)–(3) is found by applying the variational formulation (6) to the discrete solution s^h. The nodal values are then found by using the Galerkin procedure which amounts to replace $\hat{s}$ by a basis function ϕ_i in (6) for $1 \leqslant i \leqslant N$. For continuous, discontinuous and non-conforming finite element approximations, N is equal to N_V, $3N_E$ and N_S respectively. It should be noted that the localized nature of discontinuous and non-conforming approximations permits to obtain a block diagonal global mass matrix with uncoupled blocks. Hence if the time stepping of the advection and diffusion terms is explicit, the resolution of the discrete equations does not require the use of a linear solver. This is not the case with continuous approximations.

To derive the finite volume scheme, we integrate Eq. (1) on each control volume by using Green's formula and replace s by a continuous approximation s^h. The discrete equations read:

$$\int_{V_n} \frac{\partial s^h}{\partial t} \,\mathrm{d}\Omega + \int_{\partial V_n} s^h \mathbf{u} \cdot \mathbf{n} \,\mathrm{d}\Gamma = \int_{\partial V_n} K \nabla s^h \cdot \mathbf{n} \,\mathrm{d}\Gamma, \quad \text{for } 1 \leqslant n \leqslant N_V.$$

Those equations involve advective and diffusive flux budgets between control volumes. The discrete solution s^h being linear on each triangle, its values and derivatives are well defined on control volumes edges. No upwinding is thus performed while computing numerical fluxes. If s^h had been chosen to be constant on each control volume, it would have been possible to use a non-centered upwind formulation. However, this formulation has proved to be excessively diffusive.

It should be noted that the diffusion term of the non-conforming scheme can be simplified. Let us consider a node k shared by the elements Ω_i and Ω_j. The diffusion term and diffusive flux continuity constraint associated with node k can be written as:

$$\begin{aligned} A_k = &\int_{\Omega_i} K \nabla s^h \cdot \nabla \phi_k \,\mathrm{d}\Omega - \int_{\partial \Omega_i} K \nabla s^h \cdot \mathbf{n}_i \phi_k \,\mathrm{d}\Gamma + \int_{\partial \Omega_i} (K \nabla s^h_{|\Omega_i} - K \nabla s^h_{|\Omega_{nb_i}}) \cdot \mathbf{n}_i \frac{\phi_k}{2} \,\mathrm{d}\Gamma \\ &+ \int_{\Omega_j} K \nabla s^h \cdot \nabla \phi_k \,\mathrm{d}\Omega - \int_{\partial \Omega_j} K \nabla s^h \cdot \mathbf{n}_j \phi_k \,\mathrm{d}\Gamma + \int_{\partial \Omega_j} (K \nabla s^h_{|\Omega_j} - K \nabla s^h_{|\Omega_{nb_j}}) \cdot \mathbf{n}_j \frac{\phi_k}{2} \,\mathrm{d}\Gamma, \end{aligned}$$

where nb_i denotes the index of the elements neighboring Ω_i and sharing a common edge. Since the discrete solution is linear, it can be immediately observed that:

$$\int_{\Omega_{i,j}} \nabla \cdot (K \nabla s^h) \phi_k \,\mathrm{d}\Omega = \int_{\Omega_{i,j}} K \nabla s^h \cdot \nabla \phi_k \,\mathrm{d}\Omega - \int_{\partial \Omega_{i,j}} K \nabla s^h \cdot \mathbf{n}_{i,j} \phi_k \,\mathrm{d}\Gamma = 0.$$

Moreover, the gradient of s^h is constant and the integral of the diffusive flux on $\partial\Omega_i$ and $\partial\Omega_j$ is only non-vanishing on the common interface Γ_l between Ω_i and Ω_j. This is due to the non-conforming shape function ϕ_k which is equal to 1 on Γ_l and linearly varies between -1 and 1 on the other edges. Hence, all boundary integrals reduce to an integral on the common edge Γ_l. The diffusion term may thus be rewritten as:

$$\begin{aligned} A_k &= \frac{1}{2} \int_{\Gamma_l} (K \nabla s^h_{|\Omega_i} - K \nabla s^h_{|\Omega_j}) \cdot \mathbf{n}_i \phi_k \,\mathrm{d}\Gamma + \frac{1}{2} \int_{\Gamma_l} (K \nabla s^h_{|\Omega_j} - K \nabla s^h_{|\Omega_i}) \cdot \mathbf{n}_j \phi_k \,\mathrm{d}\Gamma, \\ &= \int_{\Gamma_l} K \nabla s^h_{|\Omega_i} \cdot \mathbf{n}_i \phi_k \,\mathrm{d}\Gamma + \int_{\Gamma_l} K \nabla s^h_{|\Omega_j} \cdot \mathbf{n}_j \phi_k \,\mathrm{d}\Gamma \\ &= \int_{\Omega_i} K \nabla s^h \cdot \nabla \phi_k \,\mathrm{d}\Omega + \int_{\Omega_j} K \nabla s^h \cdot \nabla \phi_k \,\mathrm{d}\Omega. \end{aligned} \tag{7}$$

So, for non-conforming approximations, the discontinuous Galerkin formulation with weak constraints on the fluxes surprisingly appears to provide the same formulation as if we had simply omitted the boundary terms while performing the integral by parts. Hence, it seems that we commit a variational crime (Thomasset, 1981), but in fact, such a formulation is perfectly equivalent to the classical one. Moreover, as the integral of $[s^h]$ vanishes along each segment, it seems reasonable to drop the solution value continuity constraint. Hence, by construction, a weak continuity is automatically achieved for linear non-conforming shape functions. Those observations in particular hold for the linear non-conforming approximation which exhibits such a nice compromise between continuous and discontinuous interpolations (Brenner and Scott, 2002).

Let us note that Eq. (7) can also be obtained by observing that the diffusion term of the non-conforming scheme at a node k shared by elements Ω_i and Ω_j can be written as

$$A_k = \int_{\Omega_i \cup \Omega_j} K \nabla s^h \cdot \nabla \phi_k \, \mathrm{d}\Omega - \int_{\partial\Omega_i \cup \partial\Omega_j} \langle K \nabla s^h \cdot \mathbf{n} \rangle [\phi_k] \, \mathrm{d}\Gamma,$$

thanks to Eq. (6). As the integral of $[\phi_k]$ vanishes all around both elements and $K\nabla s^h \cdot \mathbf{n}$ is elementwise constant, we find the same result as before.

6. About local and global conservation

In this section we show that all the methods studied in the present paper are locally conservative. It is generally admitted that finite volume and discontinuous and non-conforming finite element schemes are locally conservative. This is due to their formulation in term of flux budgets on an element basis. However continuous finite element schemes are usually said to be only globally conservative. Let us show that they are also conservative on individual elements.

We consider a generic time-dependent conservation law for a scalar quantity s:

$$\frac{\partial s}{\partial t} + \nabla \cdot \boldsymbol{\sigma} = f, \tag{8}$$

where f is a source term and $\boldsymbol{\sigma}$ is a flux function. For the problem considered in the present paper:

$$\boldsymbol{\sigma} = \mathbf{u}s - K\nabla s$$

and $f = 0$. We assume that the flux function is such that $\boldsymbol{\sigma} \cdot \mathbf{n} = 0$ on $\partial\Omega$.

Let us consider a subset Ω_e of Ω composed of one or several triangles E_i (Fig. 5) and let I_e be the ensemble of degrees of freedom in Ω_e. The discrete equations associated with Ω_e may be written as:

$$\int_\Omega \left(\phi_i \frac{\partial s^h}{\partial t} - \phi_i f - \nabla \phi_i \cdot \boldsymbol{\sigma}^h \right) \mathrm{d}\Omega + \int_{\partial\Omega} \phi_i \boldsymbol{\sigma}^h \cdot \mathbf{n} \, \mathrm{d}\Gamma = 0 \quad \forall i \in I_e,$$

where $\boldsymbol{\sigma}^h$ is the discrete flux function. The integral on Ω may be decomposed into integrals on Ω_e and $\Omega \setminus \Omega_e$:

$$\int_{\Omega_e} \left(\phi_i \frac{\partial s^h}{\partial t} - \phi_i f - \nabla \phi_i \cdot \boldsymbol{\sigma}^h \right) \mathrm{d}\Omega + \int_{\Omega \setminus \Omega_e} \left(\phi_i \frac{\partial s^h}{\partial t} - \phi_i f - \nabla \phi_i \cdot \boldsymbol{\sigma}^h \right) \mathrm{d}\Omega + \underbrace{\int_{\partial\Omega} \phi_i \boldsymbol{\sigma}^h \cdot \mathbf{n} \, \mathrm{d}\Gamma}_{=0} = 0 \quad \forall i \in I_e. \tag{9}$$

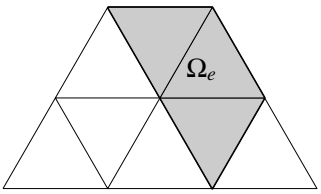

Fig. 5. Subset Ω_e (in gray) of the computational domain Ω.

The first two terms of Eq. (9) are opposed and can be interpreted as the integral of the flux $\boldsymbol{\sigma}^h \cdot \mathbf{n}$ weighted by ϕ_i along the common interface (Hughes et al., 2000). The opposed signs refer to opposed normals respectively (the flux from Ω_e to $\Omega \setminus \Omega_e$ or the flux from $\Omega \setminus \Omega_e$ to Ω_e). In other words, if we consider a local problem restricted to Ω_e and wish to obtain a local solution exactly identical to the global solution, we shall impose a flux such that its weighed integral would provide exactly the same result as the second term of Eq. (9). It is well known that an accurate calculation of fluxes along interfaces of finite element meshes has to be performed in such a way (Babuska and Miller, 1984; Gresho et al., 1987; Oshima et al., 1998). Hence Eq. (9) may be rewritten as:

$$\int_{\Omega_e} \left(\phi_i \frac{\partial s^h}{\partial t} - \phi_i f - \nabla \phi_i \cdot \boldsymbol{\sigma}^h \right) \mathrm{d}\Omega + \int_{\overline{(\Omega \setminus \Omega_e)} \cap \overline{\Omega}_e} \phi_i \boldsymbol{\sigma}^h \cdot \mathbf{n} \, \mathrm{d}\Gamma = 0 \quad \forall i \in I_e.$$

As $\boldsymbol{\sigma}^h \cdot \mathbf{n} = 0$ on $\partial\Omega$, we have:

$$\int_{\Omega_e} \left(\phi_i \frac{\partial s^h}{\partial t} - \phi_i f - \nabla \phi_i \cdot \boldsymbol{\sigma}^h \right) \mathrm{d}\Omega + \int_{\partial\Omega_e} \phi_i \boldsymbol{\sigma}^h \cdot \mathbf{n} \, \mathrm{d}\Gamma = 0 \quad \forall i \in I_e.$$

Summing all the discrete equations associated with the subset Ω_e leads to the integral form of the conservation law:

$$\frac{\mathrm{d}}{\mathrm{d}t} \int_{\Omega_e} s^h \, \mathrm{d}\Omega = \int_{\Omega_e} f \, \mathrm{d}\Omega - \int_{\partial\Omega_e} \boldsymbol{\sigma}^h \cdot \mathbf{n} \, \mathrm{d}\Gamma. \tag{10}$$

This relation implies that the total amount of s^h in Ω_e may only change due to fluxes through the domain boundary and internal sources or sinks. The quantity s^h is thus conserved locally on Ω_e. The same argument may be used for finite volumes or discontinuous and non-conforming finite element methods. Hence all the methods examined in the present paper are elementwise conservative if fluxes are computed in an appropriate way. This point has already been discussed by Berger and Howington (2002) but we found useful to dwell up on it again.

7. About dispersion

In this section we present the dispersion relation of the discontinuous finite element scheme for an advection equation. A similar analysis is performed by Danilov et al. (2003) for a continuous stabilized finite element scheme. For the sake of simplicity, we shall consider the one-dimensional advection equation with a constant advecting velocity u:

$$\frac{\partial s}{\partial t} + \frac{\partial}{\partial x}(us) = 0.$$

This equation is solved on a one-dimensional uniform grid with element size h. We seek solutions of the form $s(x,t) = \tilde{s}e^{-i\omega t+ikx}$, where k is the wave number in the x-direction, ω is the angular frequency and $\tilde{s}$ is a constant amplitude. This leads to the following dispersion relation for frequency:

$$\omega h/u = -2i - ie^{-ikh} \pm \sqrt{2 - 10e^{-ikh} - e^{-2ikh}}.$$

The latter relation is compared with the dispersion relations of the finite volume and continuous finite element schemes in Fig. 6. Those relations respectively read:

$$\omega h/u = \frac{4\sin(kh)}{3+\cos(kh)},$$
$$\omega h/u = \frac{3\sin(kh)}{2+\cos(kh)}.$$

It should be noted that it is not possible to compute the dispersion relation on the non-conforming finite element scheme as this discretization does not exist in one-dimensional.

The real part of the angular frequency shows that one of the two modes generated by the discontinuous scheme is non-physical and propagates in the wrong direction. However, as seen in the right panel, this mode is strongly damped since its imaginary part is negative for all wavelengths. As a result, it quickly disappears leaving only the physical mode. On the other hand, the physical mode generated by the discontinuous scheme has good dispersive properties since $\mathrm{Re}(\omega)$ is very close to the exact solution $\omega = uk$. Contrary to the finite volume and continuous finite element schemes, the dispersion relation of the discontinuous scheme is strictly monotonic and does not go to zero for $kh = \pi$. Hence, the speed at which energy propagates, given by the slope of the dispersion relation, is always positive and the scheme does not allow the existence of small-scale spurious oscillations. The continuous finite element and the finite volume schemes have similar dispersion curves even though the former exhibits slightly less dispersion than the latter.

The right panel shows the imaginary part of frequency. The frequencies of the exact, continuous finite element and finite volume solutions are strictly real and do not appear on the plot. The

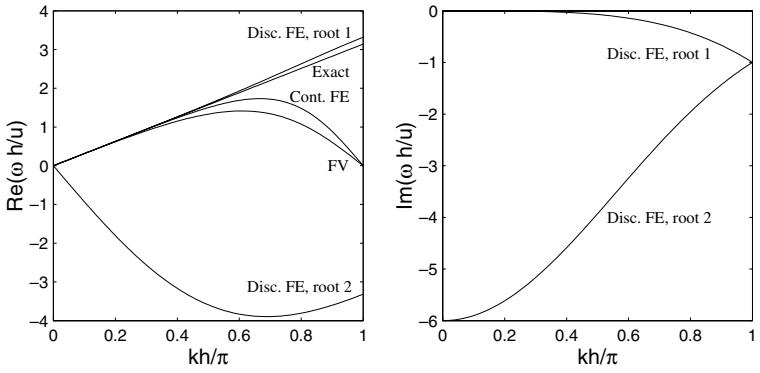

Fig. 6. Dispersion relations of the discontinuous finite element (Disc. FE), continuous finite element (Cont. FE) and finite volume (FV) schemes compared to the exact relation. The left and right panels represent the real and imaginary parts of the dispersion relation respectively.

physical mode of the discontinuous scheme is only dissipative for high frequencies which is a desirable property. Hence the upwinding introduced in the scheme only has an effect on small scale features and leaves the main solution unchanged.

8. Numerical simulations and discussion

In this section, we perform some numerical experiments to assess the different numerical schemes introduced previously. An usual test case to examine the behaviour of transport schemes is the cone rotation test. This test involves the transport of a profile containing sharp discontinuities within a smooth velocity field. Such a situation is however rare in ocean modelling where the transport of a smooth tracer field in a localized, highly sheared current is more likely to happen. That is why we consider the more realistic test problem introduced by Hecht et al. (1995).

In their paper, the authors compare different finite difference advection schemes by considering the transport of a gaussian hill through the western boundary layer of a Stommel flow. A reference solution s^r can be built at each time step through a fourth-order Runge–Kutta integration of the analytic velocity field to find the departure point corresponding to each arrival point on the grid. The same test problem is considered in Hecht et al. (2000) but for a rotated grid so that the western boundary current of the gyre is no longer aligned with one of the grid axes. This test is of course more severe for numerical schemes using a structured grid.

As an initial test, we perform Hecht's test problem by using exactly the same parameters and geometry as Hecht et al. (1995) did. Hence, we use a structured grid whose resolution is equal to the boundary layer width. This poor resolution was justified by the under-resolution of localized phenomena which often occurs in structured grid ocean models. To compare results, we compute the errors on the minimum and maximum values of the discrete solution. Those errors read:

$$e_{\min} = \min_{\Omega} s^h - \min_{\Omega} s^r,$$
$$e_{\max} = \max_{\Omega} s^h - \max_{\Omega} s^r.$$

Error measures after 1.5×10^8 s are given in Table 1. Results for the schemes we are studying are compared with some results given by Hecht et al. (1995) for the so-called CTCS (Roache, 1976), MPDATA (Smolarkiewicz, 1984) and QUICKEST (Leonard, 1979) finite difference schemes. It is clearly seen that continuous finite elements and finite volumes give poor results on low resolution structured grids. The min and max errors show that such numerical schemes produce large ripples which severely pollute the discrete solution. On the other hand, discontinuous methods perform better and give results comparable to popular finite difference advection schemes.

Nevertheless, the previous comparison is of limited interest for the methods under consideration since they allow the use of unstructured grids. As those grids permit to have a variable resolution, it is in principle always possible to have at least a few nodes in the boundary layers. So, the next numerical experiment uses an unstructured grid whose resolution is sufficient to avoid under-resolved boundary layers (Fig. 7). However, the resolution of the grid is not optimal since in practice this is not always affordable. For instance, commonly used viscosity values give western boundary widths ranging from 30 to 200 km (Yang, 2003). An accurate representation of each boundary layer may thus be hard to achieve in a global circulation model, even with variable

Table 1
Errors on the mininum and maximum values after 1.5×10^8 s

Scheme	Comments	$e_{\min}$	$e_{\max}$
Finite volumes	Centered in space, leap frog	−1.29	0.28
Continuous finite elements	Centered in space, leap frog	−1.75	0.72
Discontinuous finite elements	Upwind advective fluxes, Euler	−0.16	−0.22
Non-conforming finite elements	Upwind advective fluxes, Euler	−0.29	−0.31
Finite differences CTCS	Centered in space, leapfrog	−0.64	−0.31
Finite differences MPDATA	Fully multidimensional iterative scheme two iterations (one antidiffusive iteration)	−0.09	−0.45
Finite differences QUICKEST	Operator split implementations with and without compensation of velocity gradient error terms	−0.04	−0.49

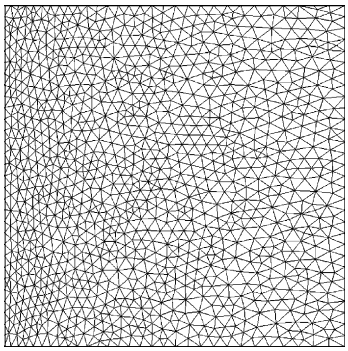

Fig. 7. Unstructured mesh used for the gaussian hill transport simulation. This mesh has 2222 elements and there are approximately five elements in the boundary layer.

resolution. Therefore, for the present grid, there are five elements in the boundary layer which is a compromise between low and high resolution.

The computational domain is a square $L \times L$ basin ($L = 10^6$ m) and we consider a Stommel flow of which streamfunction is:

$$\Psi(x,y) = \frac{FL}{\pi\gamma\rho H}\sin\left(\frac{\pi y}{L}\right)(p\mathrm{e}^{xz_+} + q\mathrm{e}^{xz_-} - 1),$$

where $0 \leqslant x, y \leqslant L$. The amplitude of the wind stress is $F = 0.1$ N/m^2, the frictional coefficient is $\gamma = 10^{-6}$ s^{-1}, the fluid layer density is $\rho = 1000$ kg/m^3 and the fluid layer depth is $H = 200$ m. The arguments and amplitudes of the exponential functions are

$$z_\pm = -\frac{\alpha}{2} \pm \sqrt{\frac{\alpha^2}{4} + \left(\frac{\pi}{L}\right)^2},$$
$$p = \frac{1-\mathrm{e}^{Lz_-}}{\mathrm{e}^{Lz_+} - \mathrm{e}^{Lz_-}},$$
$$q = 1 - p,$$

where $\alpha = \beta/\gamma$ and β is the Coriolis factor first-order derivative. The boundary layer width is of order of $\alpha^{-1} = 100$ km. The velocity $\mathbf{u} = (u, v)$ is found from the streamfunction:

$$u = \frac{\partial \Psi}{\partial y} \quad \text{and} \quad v = -\frac{\partial \Psi}{\partial x}.$$

The advection and diffusion terms are both discretized explicitly in time and the time step is set to 2500 s. A centered leap frog scheme is used with centered spatial discretizations of purely advective flows. An Euler backward scheme is used in any other case. The initial tracer field is given by the following expression:

$$s_0(x, y) = 10 \exp\left(- \frac{((x - 2L/3)^2 + (y - L/3)^2)}{2(L/12.5)^2} \right).$$

The stream function of the flow and the initial tracer field are represented on Fig. 8.

The L_2 error between the discrete and the reference solution is computed for a more quantitative comparison. It is defined as:

$$e_{L_2} = \frac{\|s^r - s^h\|_{L_2(\Omega)}}{\|s^r\|_{L_2(\Omega)}},$$

where $\| \cdot \|_{L_2(\Omega)}$ is the L_2 norm on Ω. The min and max errors are also computed in order to estimate the importance of unphysical extrema generated by the numerical model.

8.1. Pure advection

We first study the transport of the tracer in a purely advective flow. The grid being totally unstructured, elements are not aligned with the boundary layer current and the experiment is thus

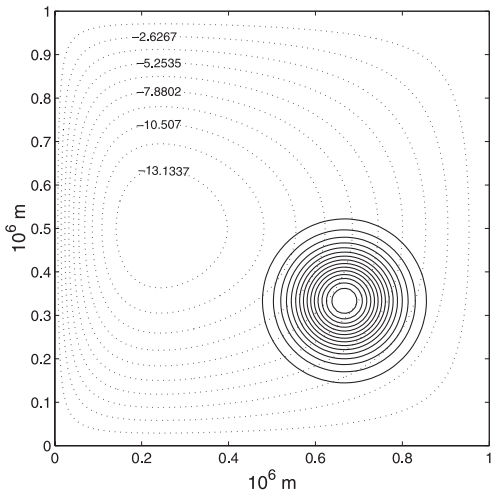

Fig. 8. Stream function (in sverdrups) of the flow (dotted line) and initial tracer distribution (solid line). The orientation of the flow is clockwise.

comparable to that performed by Hecht et al. (2000). Results for the different schemes are presented in Fig. 9 at different stages of the gaussian hill displacement. Error measures are given in Fig. 10.

Before the tracer field gets in the boundary layer, all schemes give similar results. Afterward, the L_2 error increases significantly for each scheme when the tracer goes through the boundary current. This increase is however more important for schemes using continuous approximations. When the tracer has left the boundary layer, the error committed by continuous schemes is more

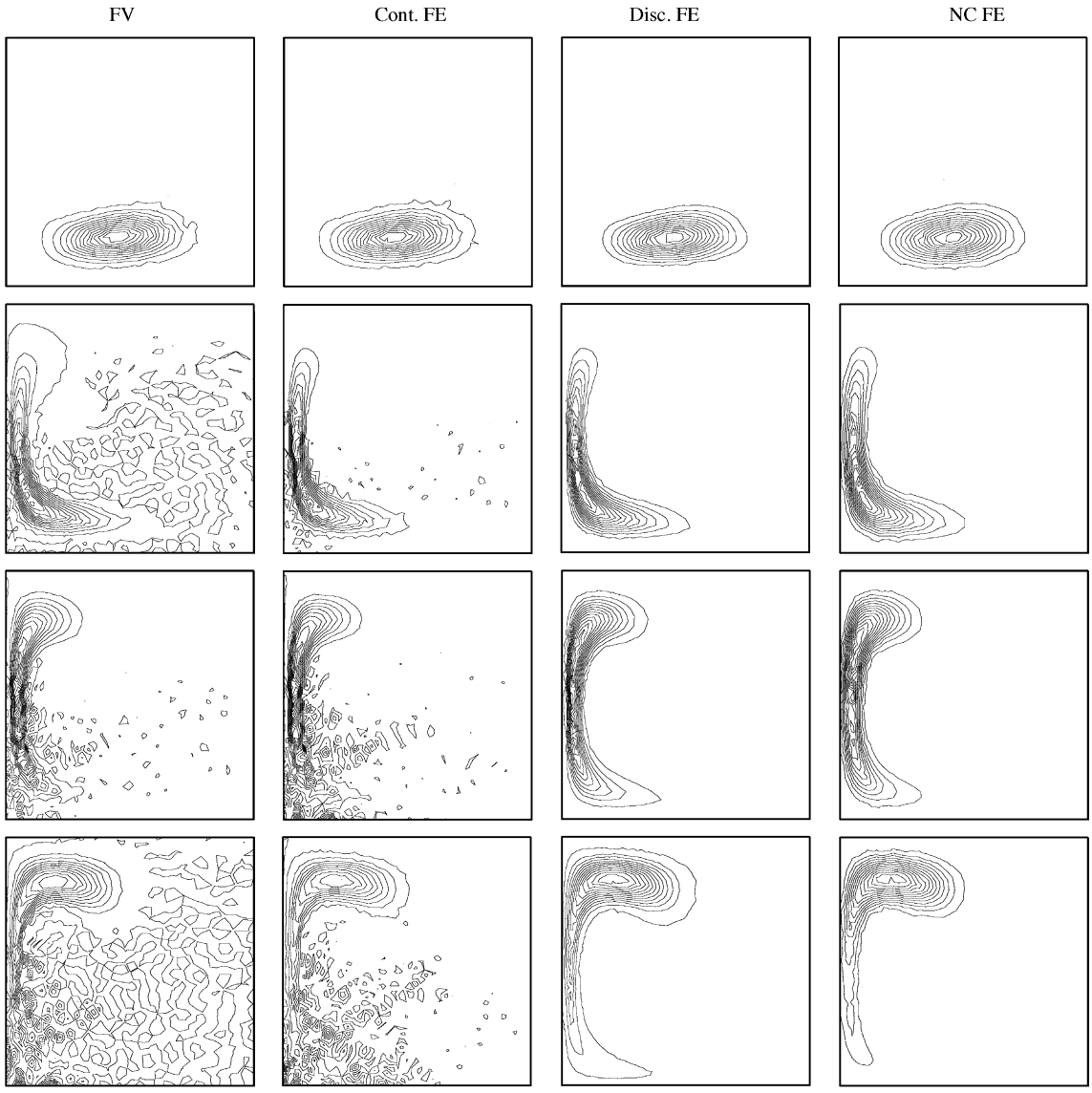

Fig. 9. Snapshots of the simulated tracer field after 2×10^6, 4×10^6, 5×10^6 and 6×10^6 s respectively for pure advection with the finite volume (FV), continuous finite element (Cont. FE), discontinuous finite element (Disc. FE) and nonconforming finite element (NC FE) schemes. There are 13 isolines.

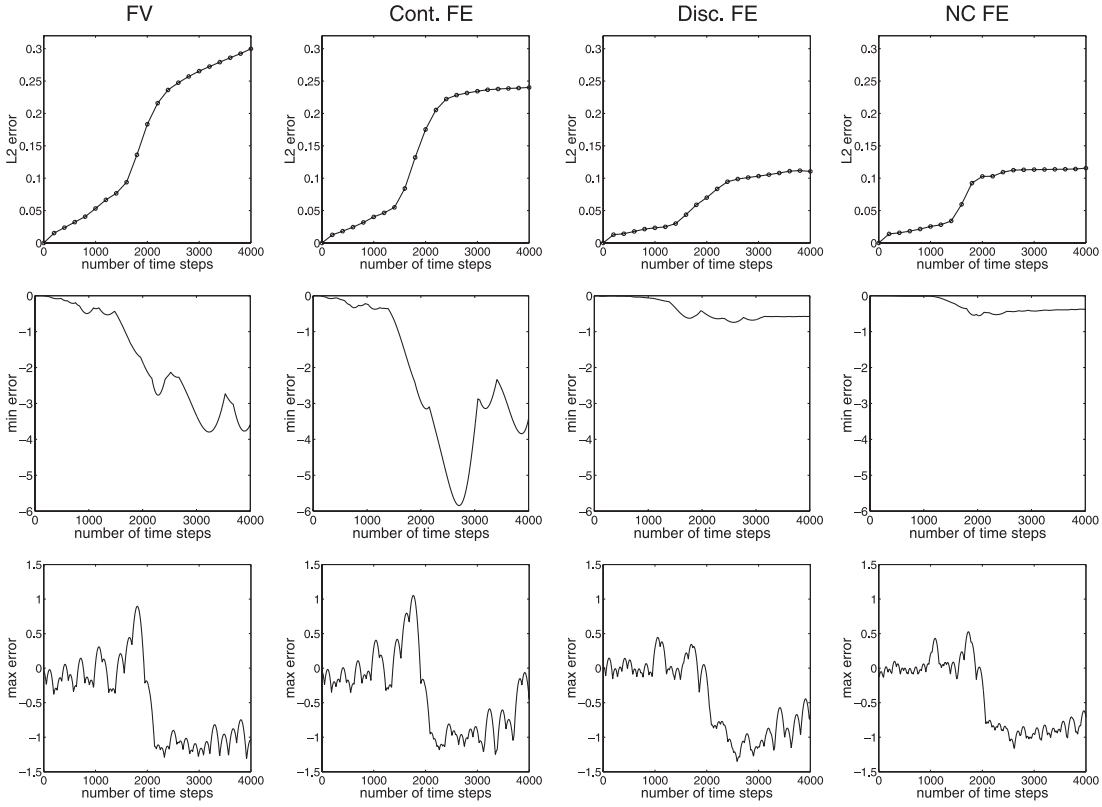

Fig. 10. L_2 (top), min (middle) and max (bottom) errors resulting from pure advection of the tracer profile.

than twice larger than for discontinuous or non-conforming schemes. This is due to the lack of flexibility of continuous methods which prevents them from representing accurately solutions with steep gradients. As a result, they are prone to produce ripples that propagate in the domain and reflect on boundaries. An estimation of the ripples importance is given by the min error (Fig. 10). Hence for the finite element scheme, the largest downward ripple is nearly 60% as large as the initial peak value. There are yet stabilization procedures such as streamline diffusion or least-squares stabilization (Hughes et al., 1989) that can be used to avoid unphysical extrema but they may have an important diffusive effect.

On the other hand discontinuous and non-conforming finite element schemes perform better. Their higher flexibility enables a more accurate representation of the solution in the boundary layer. The upwind-weighted formulation shows good shape preservation and much reduced rippling (Fig. 10). It must be pointed out that the upwind formulation does not have an important diffusive effect as the peak value of the tracer distribution does not decrease much (Fig. 10). Moreover the L_2 error stays constant when the tracer has left the boundary current which shows that upwinding has a negligible impact on the main solution.

It should be noted that the advection schemes studied in the present paper are not monotonic by design. This is clearly seen on Fig. 10. Standard flux or solution limiters can be applied to the numerical solutions so as to render them monotonic. However, the use of such limiters will make

the comparison of our schemes not so highlighting. Moreover the careful selection of suitable numerical parameters for such schemes needs further researches.

8.2. Advection and diffusion

Since ocean modelling is not a purely advective problem, it is interesting to see what happens if a physically realistic diffusivity is included. For the grid used in the present simulation, the average

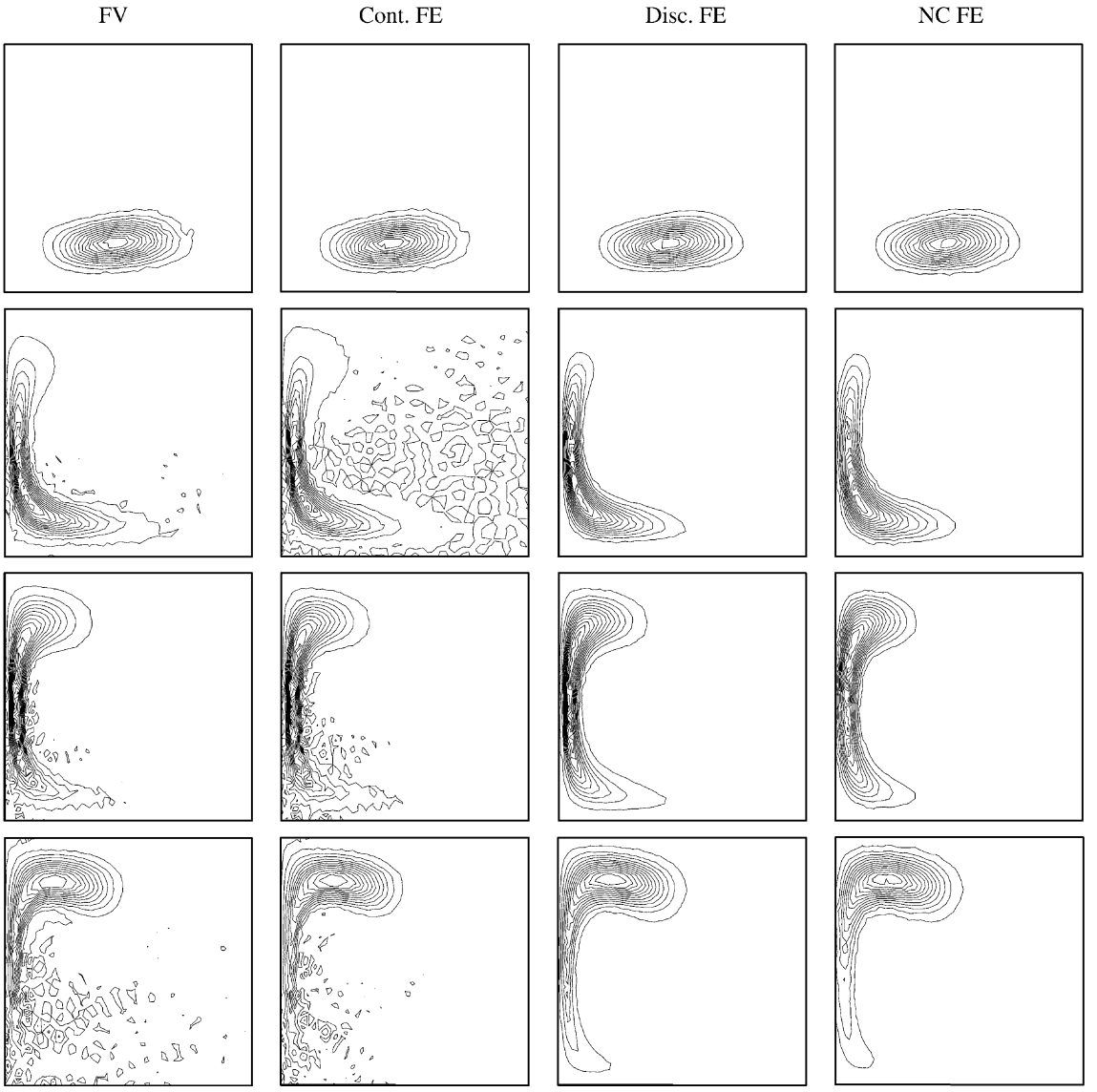

Fig. 11. Snapshots of the simulated tracer field after 2×10^6, 4×10^6, 5×10^6 and 6×10^6 s respectively for advection–diffusion ($K = 30$ m^2/s) with the finite volume, continuous finite element, discontinuous finite element and non-conforming finite element schemes. There are 13 isolines.

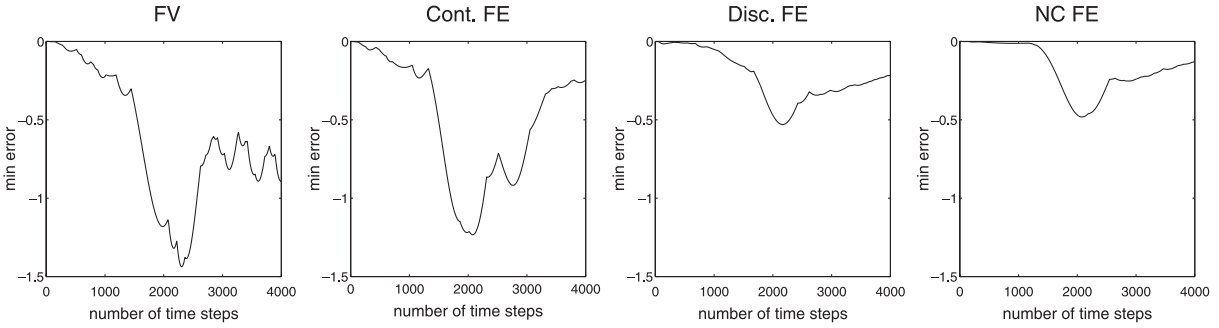

Fig. 12. Min errors resulting from advection–diffusion of the tracer profile.

size of an element is of the order of 30 km. Hence, according to Okubo (1971), a Laplacian diffusivity of 30 m^2/s should be used. The same numerical simulation as before is performed. Snapshots of the tracer distribution are presented in Fig. 11.

Results are now slightly better for the continuous finite element and finite volume schemes. Ripples have decreased but not disappeared and the tracer distribution is still very noisy. A much higher level of diffusion is needed to totally filter out oscillations. Discontinuous and non-conforming finite elements still give good results and the largest downward ripples are only 5% as large as the initial peak amplitude (Fig. 12). As diffusion increases, all schemes tend to give similar results.

Finally, it should be noted that the comparison performed here could appear biased as the numerical schemes under consideration do not have the same number of degrees of freedom. Discontinuous and non-conforming approximations respectively have six and three times more degrees of freedom than continuous approximations. However discontinuous and non-conforming schemes do not require linear solvers and their computational cost thus is comparable to continuous schemes. In our implementation, continuous finite elements are the cheapest method but the other schemes are no more than 25% more expensive.

9. Conclusions

Discontinuous and non-conforming finite element schemes are well suited to advection dominated flows. The high flexibility inherent in those methods permit to represent accurately solutions with steep gradients. They naturally allow upwind-weighted formulations that greatly reduce unphysical oscillations usually generated by centered schemes. Such upwind formulations allow much smaller diffusivities that are in better accord with observations.

Usual continuous finite element and finite volume schemes have difficulties to represent advection dominated flows and are prone to generate ripples in regions with strong shear. A level of diffusion beyond physically realistic values is needed to avoid oscillations. Despite a smaller number of degrees of freedom, the computational cost of continuous methods is comparable to the one of discontinuous or non-conforming methods since the latter do not require linear solvers.

Obviously, some improvement could be obtained by introducing upwinding in continuous schemes but such an investigation is beyond the scope of this work.

Therefore, discontinuous and non-conforming finite elements appear to be the most promising approximations to represent the evolution of scalar quantities in oceanic flows. Those schemes combine different properties such as flexibility, local conservation, upwinding and reasonable computational cost that would be particularly useful in ocean modelling.

Acknowledgements

Emmanuel Hanert and Eric Deleersnijder are Research fellow and Research associate, respectively, with the Belgian National Fund for Scientific Research (FNRS). The support of the Convention d'Actions de Recherche Concertées ARC 97/02-208 with the Communauté Française de Belgique is gratefully acknowledged. Daniel Y. Le Roux is supported by grants from the Natural Sciences and Engineering Research Council (NSERC) and the Fonds Québécois de la Recherche sur la Nature et les Technologies (FQRNT).

Appendix A. Details on the variational formulation derivation

In this section we explain with more details some aspects of the derivation of the variational formulation of problem (1). We first consider the derivation of the diffusion boundary integral introduced in Eq. (4). By integrating the diffusion term by parts, we have:

$$\sum_{i=1}^{N_\Omega} \int_{\Omega_i} \nabla \cdot (K \nabla s) \hat{s} \, \mathrm{d}\Omega = -\sum_{i=1}^{N_\Omega} \int_{\partial\Omega_i} K \nabla s \cdot \mathbf{n}_i \hat{s} \, \mathrm{d}\Gamma + \sum_{i=1}^{N_\Omega} \int_{\Omega_i} K \nabla s \cdot \nabla \hat{s} \, \mathrm{d}\Omega.$$

As we restrict ourselves to homogeneous Neumann boundary conditions, the boundary integral may be rewritten as:

$$\begin{aligned}
\sum_{i=1}^{N_\Omega} \int_{\partial\Omega_i} K \nabla s \cdot \mathbf{n}_i \hat{s} &= \sum_{l=1}^{N_\Gamma} \int_{\Gamma_l} K \nabla s_{|\Omega_i} \cdot \mathbf{n}_i \hat{s}_{|\Omega_i} + K \nabla s_{|\Omega_j} \cdot \mathbf{n}_j \hat{s}_{|\Omega_j} \, \mathrm{d}\Gamma \\
&= \sum_{l=1}^{N_\Gamma} \int_{\Gamma_l} K \nabla s_{|\Omega_i} \cdot \mathbf{n} \hat{s}_{|\Omega_i} - K \nabla s_{|\Omega_j} \cdot \mathbf{n} \hat{s}_{|\Omega_j} \, \mathrm{d}\Gamma \\
&= \sum_{l=1}^{N_\Gamma} \int_{\Gamma_l} \langle K \nabla s \cdot \mathbf{n} \rangle [\hat{s}] + [K \nabla s \cdot \mathbf{n}] \langle \hat{s} \rangle \, \mathrm{d}\Gamma,
\end{aligned}$$

where $\mathbf{n}_i$ and $\mathbf{n}_j$ are the unit normal vectors pointing out of Ω_i and Ω_j respectively. The unique unit normal vector to the segment Γ_l, between Ω_i and Ω_j, is $\mathbf{n} = \mathbf{n}_i$ since $i > j$. The last integral has been derived thanks to the following relation:

$$ac - bd = \frac{1}{2}(a+b)(c-d) + \frac{1}{2}(a-b)(c+d),$$

where a, b, c and d are real numbers. The derivation of the advection boundary integral is similar.

Now we examine the continuity constraints introduced in Eq. (5). If the subdomains neighboring Ω_i and sharing a common edge are denoted Ω_{nb_i}, the continuity of the solution s between subdomains may be expressed weakly as:

$$\sum_{i=1}^{N_\Omega} \int_{\partial\Omega_i} (s_{|\Omega_i} - s_{|\Omega_{nb_i}}) a(\hat{s})\, \mathrm{d}\Gamma = \sum_{l=1}^{N_\Gamma} \int_{\Gamma_l} a(\hat{s})_{|\Omega_i} (s_{|\Omega_i} - s_{|\Omega_j}) + a(\hat{s})_{|\Omega_j} (s_{|\Omega_j} - s_{|\Omega_i})\, \mathrm{d}\Gamma$$
$$= \sum_{l=1}^{N_\Gamma} \int_{\Gamma_l} [s][a(\hat{s})]\, \mathrm{d}\Gamma = 0.$$

Likewise, the diffusive flux continuity constraint may be written as:

$$\sum_{i=1}^{N_\Omega} \int_{\partial\Omega_i} (K\nabla s_{|\Omega_i} - K\nabla s_{|\Omega_{nb_i}}) \cdot \mathbf{n}_i b(\hat{s})\, \mathrm{d}\Gamma = \sum_{l=1}^{N_\Gamma} \int_{\Gamma_l} b(\hat{s})_{|\Omega_i} (K\nabla s_{|\Omega_i} - K\nabla s_{|\Omega_j}) \cdot \mathbf{n}_i$$
$$+ b(\hat{s})_{|\Omega_j} (K\nabla s_{|\Omega_j} - K\nabla s_{|\Omega_i}) \cdot \mathbf{n}_j\, \mathrm{d}\Gamma$$
$$= \sum_{l=1}^{N_\Gamma} \int_{\Gamma_l} [K\nabla s \cdot \mathbf{n}] 2\langle b(\hat{s}) \rangle\, \mathrm{d}\Gamma = 0.$$

References

Babuska, I., Miller, A., 1984. The post-processing approach in the finite element method. 1. Calculation of displacements, stresses and other higher derivatives of the displacement. International Journal for Numerical Methods in Fluids 20, 1085–1109.

Berger, R.C., Howington, S.E., 2002. Discrete fluxes and mass balance in finite elements. Journal of Hydraulic Engineering 87, 87–92.

Brenner, S.C., Scott, L.R., 2002. The mathematical theory of finite element methods. In: Texts in Applied Mathematics, vol. 15. Springer-Verlag.

Cockburn, B., Karniadakis, G.E., Shu, C.W., 2000. Discontinuous Galerkin Methods. Theory, Computation and Applications. In: Lecture Notes in Computational Science and Engineering. Springer.

Crouzeix, M., Raviart, P., 1973. Conforming and nonconforming finite-element methods for solving the stationary stokes equations. R.A.I.R.O. Analyse Numérique 7, 33–76.

Danilov, S., Kivman, G., Schröter, J., 2003. A finite element ocean model: principles and evaluation. Ocean Modelling, in press.

Gresho, P., Lee, R., Sani, R., Maslanik, M., Eaton, B., 1987. The consistent Galerkin FEM for computing derived boundary quantities in thermal and/or fluids problems. International Journal for Numerical Methods in Fluids 7, 371–394.

Hecht, M.W., Holland, W.R., Rasch, P.J., 1995. Upwind-weighted advection schemes for ocean tracer transport: an evaluation in a passive tracer context. Journal of Geophysical Research 100, 20763–20778.

Hecht, M.W., Wingate, B.A., Kassis, P., 2000. A better, more discriminating test problem for ocean tracer transport. Ocean Modelling 2, 1–15.

Houston, P., Schwab, C., Suli, E., 2000. Discontinuous *hp*-finite element methods for advection diffusion problems. Technical Report, NA-00/15, Oxford University.

Hua, B.L., Thomasset, F., 1984. A noise-free finite element scheme for the two-layer shallow water equations. Tellus 36A, 157–165.

Hughes, T.J.R., Franca, L.P., Hubert, G.M., 1989. A new finite element formulation for computational fluid dynamics: VIII. The Galerkin-least-squares method for advective–diffusive equations. Computer Methods in Applied Mechanics an Engineering 73, 173–189.

Hughes, T.J.R., Engel, G., Mazzei, L., Larson, M.G., 2000. The continuous Galerkin method is locally conservative. Journal of Computational Physics 163, 467–488.

Leonard, B.P., 1979. A stable and accurate convective modelling procedure based on quadratic upstream interpolation. Computer Methods in Applied Mechanics and Engineering 19, 59–98.

Le Provost, C., Bernier, C., Blayo, E., 1994. A comparison of two numerical methods for integrating a quasi-geostrophic multilayer model of ocean circulations: finite element and finite difference methods. Journal of Computational Physics 110, 341–359.

Le Roux, D.Y., 2003. Analysis of the P_1^{NC}—P_1 finite-element pair in shallow-water ocean models. Monthly Weather Review, submitted for publication.

Le Roux, D.Y., Staniforth, A., Lin, C.A., 2000. A semi-implicit semi-lagrangian finite-element shallow-water ocean model. Monthly Weather Review 128, 1384–1401.

Le Saint, P., Raviart, P., 1974. On the finite element method for solving the neutron transport equation. In: de Boor, C. (Ed.), Mathematical Aspects of Finite Elements in Partial Differential Equations. Academic Press, New York, pp. 89–145.

Le Veque, R., 2002. Finite Volume Methods for Hyperbolic Problems. Cambridge University Press, Cambridge.

Lynch, D.R., Ip, J.T.C., Naimie, C.E., Werner, F.E., 1996. Comprehensive coastal circulation model with application to the Gulf of Maine. Continental Shelf Research 16, 875–906.

Myers, P.G., Weaver, A.J., 1995. A diagnostic barotropic finite-element ocean circulation model. Journal of Atmospheric and Oceanic Technology 12, 511–526.

Nechaev, D., Schröter, J., Yaremchuk, M., 2003. A diagnostic stabilized finite-element ocean circulation model. Ocean Modelling 5, 37–63.

Okubo, A., 1971. Oceanic diffusion diagrams. Deep Sea Research 18, 789–802.

Oshima, M., Hughes, T.J.R., Jansen, K., 1998. Consistent finite element calculation of boundary and internal fluxes. International Journal of Computational Fluid Dynamics 9, 227–235.

Roache, P.J., 1976. Computational Fluid Dynamics. Hermosa, Albuquerque, NM.

Smolarkiewicz, P.K., 1984. A fully multidimensional positive definite advection transport algorithm with small implicit diffusion. Journal of Computational Physics 54, 325–362.

Thomasset, F., 1981. Implementation of Finite Element Methods for Navier–Stokes Equations. In: Springer Series in Computational Physics. Springer-Verlag.

Yang, J., 2003. On the importance of resolving the western boundary layer in wind-driven ocean general circulation models. Ocean Modelling 5, 357–379.